

SIMULTANEOUS FAR-INFRARED, NEAR-INFRARED, AND
RADIO OBSERVATIONS OF OH/IR STARSM. W. WERNER,¹ S. BECKWITH, I. GATLEY, K. SELLGREN

Department of Physics, California Institute of Technology

G. BERRIMAN

Hale Observatories, California Institute of Technology

AND

D. L. WHITING

Department of Physics, California Institute of Technology

Received 1979 July 9; accepted 1980 January 22

ABSTRACT

Simultaneous far-infrared, near-infrared, and radio observations have been made of five infrared stars which show OH maser emission at 1612 MHz. These stars have very thick circumstellar dust shells and are not seen optically. The data permit a direct comparison of the far-infrared and maser emission from these sources, which strongly supports the hypothesis that the maser emission is pumped by 35 μm photons. A comparison with data obtained at earlier epochs suggests that the maser emission is saturated. The infrared and radio data are used together with estimates of the source distances to determine the luminosities and mass loss rates for these objects. The luminosities lie in the range 2×10^3 to $3 \times 10^4 L_{\odot}$ and are consistent with either Mira variable or M supergiant classifications for the underlying stars. The estimated mass loss rates lie between 5×10^{-6} and $7 \times 10^{-5} M_{\odot} \text{ year}^{-1}$.

Subject headings: infrared: sources — stars: circumstellar shells — stars: late-type — stars: mass loss

I. INTRODUCTION

Observations of both thermal and maser emission from molecules in circumstellar shells around evolved stars have been used by radio astronomers to probe the later stages of stellar evolution and to study the return of material to the interstellar medium. Molecular emission is generally associated with intrinsically cool stars, and the circumstellar shells often contain appreciable amounts of dust. Thus, the stars emit significant or dominant portions of their luminosity at infrared wavelengths, and infrared observations have been an important complement to radio studies of these systems.

Perhaps the best studied objects of this type are the OH/IR stars. These stars emit in the OH maser line at 1612 MHz, showing a characteristic double-peaked velocity profile, which is probably caused by maser emission arising from the front and back surfaces of a shell expanding uniformly around the central star. Hyland *et al.* (1972) showed that the optically visible OH/IR stars are cool, luminous late-type stars which can be identified either as Mira variables or as M supergiants. Harvey *et al.* (1974) demonstrated that the infrared and OH emission from the OH/IR stars

vary in phase; this provided very strong evidence that the maser emission was pumped radiatively.

Surveys at radio wavelengths, such as those of Winnberg *et al.* (1973), Caswell and Haynes (1975), Johansson *et al.* (1977), Bowers (1978), and Baud (1978), can identify candidate OH/IR stars at distances of many kiloparsecs by virtue of their characteristic OH emission spectra, which can also be used to determine the stellar velocities. Studies of objects discovered in radio surveys are therefore a potentially useful tool for the study of the late phases of stellar evolution throughout the Galaxy. The first infrared studies of such objects were carried out by Schultz, Kreysa, and Sherwood (1976) and by Evans and Beckwith (1977). Evans and Beckwith (hereafter EB) discovered infrared counterparts for six double-peaked 1612 MHz sources from the list of Winnberg *et al.* (1973). These infrared objects have no optical counterparts; they appear to be stars with denser dust shells than those associated with the optically visible Mira variables and M supergiants. The results of simultaneous near-infrared ($1.6 \mu\text{m} \leq \lambda \leq 12.5 \mu\text{m}$), far infrared ($\lambda \geq 25 \mu\text{m}$), and 1612 MHz OH observations of five of these six sources are presented in this paper. Because these stars vary by more than a factor of 2 at both near-infrared and radio wavelengths on time scales of ~ 1 year, the simultaneous measurements are necessary if the results obtained in the

¹ Also at Hale Observatories, California Institute of Technology. The Hale Observatories are operated jointly by the Carnegie Institution of Washington and the California Institute of Technology.

different spectral bands are to be compared. The principal new feature of this work is the addition of the far-infrared measurements, which have been compared with the simultaneous OH measurements in the first quantitative test of the hypothesis that the maser emission is pumped by $35\ \mu\text{m}$ radiation. In addition, the data give an observational description of the objects, which is complete for one epoch. This allows a determination of the luminosities, shell masses, and mass loss rates for these stars and a comparison of their infrared energy distributions with the results of model calculations for dust-embedded stars.

In § II below, the observational techniques are described, and the main results are presented in § III. The infrared energy distributions and the results concerning the pumping mechanism, which are independent of distance, are discussed in § IV. In § V, kinematic arguments are used to estimate the distances, and, therefore, the total luminosities of these stars. The luminosity estimates form the basis for estimates of the mass loss rates. In § VI, the properties of the circumstellar shells are determined by comparing the data with existing models of systems of this type, and the main conclusions of this work are summarized in § VII. An independent study of near- and far-infrared emission from a number of OH/IR stars has been carried out by Telesco *et al.* (1980). For the one source observed in common, OH 26.5+0.6, the measurements are in good agreement, and the overall results and conclusions of both works are consistent.

II. OBSERVATIONS

The observations described here were made during 1978 July and August. The OH observations were made July 17–18, the far-infrared observations July 20, and the near-infrared observations July 25–28, except for OH 30.1–0.2, which was observed in the near-infrared on August 27. EB found that these sources are fairly constant over a period of a month. Since the bulk of the data were taken over an 11 day period, and since the far-infrared and OH measurements (for which a quantitative comparison is of the greatest interest) were separated by less than 3 days, all data on each source are treated as simultaneous.

a) Near-Infrared Observations ($1.6\ \mu\text{m} < \lambda < 12.5\ \mu\text{m}$)

The near-infrared observations were made using the 1.5 m telescope at Mount Wilson. The measurements at $\lambda \leq 4.8\ \mu\text{m}$ were made using the InSb detector system described by Becklin *et al.* (1978) with a $13''$ aperture, while the measurements in the $10\ \mu\text{m}$ region were made using the Ge bolometer system described by Beckwith *et al.* (1976) with a $9''$ aperture. In each case, emission from the sky was subtracted by chopping $30''$ in right ascension. The uncertainties in the near-infrared measurements, as determined by a com-

bination of calibration and statistical errors, are $\pm 15\%$.

b) Far-Infrared Measurements ($\lambda > 25\ \mu\text{m}$)

The far-infrared measurements were made using the 91 cm telescope of NASA's Kuiper Airborne Observatory. The detector was a Ge bolometer with a $30''$ field of view. Emission from the sky was subtracted by chopping $2'$ in azimuth; this corresponded approximately to an east-west direction on the sky.

Each source was measured through both (1) an interference filter with a $25\text{--}35\ \mu\text{m}$ bandpass and (2) a broadband system which had a $45\ \mu\text{m}$ short wavelength cut-on determined by CaF_2 and sapphire transmission filters and a cutoff at $\sim 130\ \mu\text{m}$ due to diffraction. The far-infrared measurements were calibrated by observations of NGC 7027 and of the compact source in S140, for which the far-infrared energy distributions as given by Telesco and Harper (1977), and Harvey, Campbell, and Hoffman (1978) were adopted. It was assumed that the $\lambda \geq 25\ \mu\text{m}$ spectrum of each OH/IR star could be fitted by a single Planck curve. The calibration was carried out by integrating the known spectra of the calibration sources over the filter bandpasses and using the results to predict the ratio of signals which would be observed using the two bandpasses for blackbodies of various temperatures. For each OH/IR source, the observed ratio of signals in the two bandpasses then defined a far-infrared color temperature T_F ; this temperature and the strength of the signals determined the monochromatic fluxes which, for convenience, were referred to wavelengths of $30\ \mu\text{m}$ and $50\ \mu\text{m}$ for the $25\text{--}35\ \mu\text{m}$ and $45\text{--}130\ \mu\text{m}$ systems, respectively. It was assumed in the calibration that the OH/IR stars are spatially unresolved by the $30''$ beam used for the far-infrared observations. This was established directly by spatial scanning of OH 26.5+0.6 at $30\ \mu\text{m}$; it is also consistent with the models of these objects described below. The overall uncertainty in the far-infrared measurements, which is due primarily to the calibration uncertainties, is estimated to be $\pm 30\%$.

c) OH Emission Observations at 1612 MHz

Observations of the OH emission at 1612 MHz were made using the 40 m antenna at the Owens Valley Radio Observatory. Each measurement was made by integrating at the position of the maser with a beam size of $20''$; integrations at a position 1° away from each maser were made to establish a baseline. A 100 channel autocorrelator was used to give a velocity resolution of $0.5\ \text{km s}^{-1}$. For spectral features which were unresolved at this spectral resolution, additional measurements were made with $0.1\ \text{km s}^{-1}$ resolution to determine the flux densities. Each maser was observed at least twice to check the internal consistency of the measurements. A noise tube was used to calibrate the signal strengths; known continuum sources were observed to establish the overall flux

TABLE 1
INFRARED DATA—1978 JULY

A. MEASURED FLUXES ^a (Jy)											
Source ^b	1.6 μm	2.2 μm	3.4 μm	4.8 μm	10.1 μm	8.7 μm	9.5 μm	11.2 μm	12.5 μm	30 μm	50 μm
OH 45.5+0.1	0.15	0.75	7	12	18	21	19	21	21	40	60 ^c
OH 30.1-0.2	0.35	3	18	30	48	48	35	45	58	35	25
OH 26.5+0.6	0.007	0.3	75	200	280	325	130	200	660	845	580
OH 21.5+0.5	<0.006	2	14	18	30	9	10	48	120	110
OH 32.8-0.3	<0.006	0.45	4	10	13	4	4	23	80	75

B. DERIVED QUANTITIES				
SOURCE	COLOR TEMPERATURES (K)		TOTAL FLUX RECEIVED (W m^{-2})	FLUX ($\lambda \geq 25 \mu\text{m}$)/ TOTAL FLUX
	T_N (3.4–12.5 μm)	T_F (30–50 μm)		
OH 45.5+0.1	640	100	2×10^{-11}	0.20
OH 30.1-0.2	630	200	4×10^{-11}	0.10
OH 26.5+0.6	515	200	3.5×10^{-10}	0.15
OH 21.5+0.5	435	150	3×10^{-11}	0.30
OH 32.8-0.3	400	150	1.5×10^{-11}	0.40

^a Typical uncertainties in fluxes: $\pm 15\%$, $\lambda \leq 12.5 \mu\text{m}$; $\pm 30\%$, $\lambda \geq 30 \mu\text{m}$. Upper limits are 2σ .

^b To facilitate comparison, the sources are listed in the tables in the same order in which they appear in Fig. 1.

^c The 50 μm flux from OH 45.5+0.1 may include contribution from adjacent H II region G 45.5+0.1 (Zeilik *et al.* 1975).

density scale. The uncertainty in the flux densities is estimated to be 5% (1 σ) with the major uncertainties coming from baseline subtraction and flux calibration.

III. RESULTS

The results of the infrared measurements are listed in Table 1 which shows the infrared flux densities, the near-infrared (3.4–12.5 μm) color temperature, T_N , and the far-infrared color temperature, T_F . The infrared energy distributions are plotted in Figure 1; as is shown for OH 32.8–0.3, the energy distributions can be approximated by the superposition of two Planck curves at the color temperatures T_N and T_F , with the addition of a silicate absorption feature at 10 μm . The strength of this feature varies markedly from one OH source to another.

The 1612 MHz OH emission spectra of the sources, shown in Figure 2, exhibit characteristic double-peaked velocity profiles. The results of the OH measurements are given in Table 2, which lists the velocity spacing, ΔV , between the two peaks and the peak OH flux density, $S_v(\text{OH})$, which is the average of the peak flux densities in the two OH velocity peaks.

The present data can be compared with the near-infrared and OH observations obtained by EB in 1975 June–July. Variability of both near-infrared and OH fluxes by at least a factor of 2 is seen for three sources: OH 26.5+0.6, OH 32.8–0.3, and OH 45.5+0.1. The variations are correlated; in each case, the sense of the change in the flux density is the same at all near-infrared wavelengths and in the OH line. Specifically, OH 26.5+0.6 and OH 45.5+0.1 were brighter in 1978 than in 1975, while OH 32.8–0.3 was fainter. The

other two sources, OH 21.5+0.5 and OH 30.1–0.2, had the same peak OH intensity in 1978 as in 1975. In the near infrared, OH 21.5+0.5 was $\sim 25\%$ brighter in 1978 than in 1975, while the near-infrared flux of OH 30.1–0.2 decreased by a similar factor.

IV. DISCUSSION OF DISTANCE-INDEPENDENT QUANTITIES

a) Infrared Energy Distributions

The breadth of the energy distributions shown in Figure 1 and the fact that T_F is less than T_N for each object indicate that there is a range of dust temperatures in the circumstellar shells, with the far-infrared emission coming primarily from cooler dust which is, presumably, at greater distances from the stars. The ratio of far-infrared ($\lambda \geq 25 \mu\text{m}$) flux to total flux for the five sources ranges from 0.1 to 0.4 (Table 1). Thus the bulk of the luminosity of these stars is not emitted in the far infrared.

b) Pumping of the Maser Emission

The correlated variations of OH and infrared flux densities observed for these sources support the idea

TABLE 2
OH DATA—1978 JULY

Source	ΔV (km s^{-1})	$S_v(\text{OH})$
OH 45.5+0.1	34	10.0
OH 30.1-0.2	35	14.3
OH 26.5+0.6	28	290
OH 21.5+0.5	37	23
OH 32.8-0.3	30	13.0

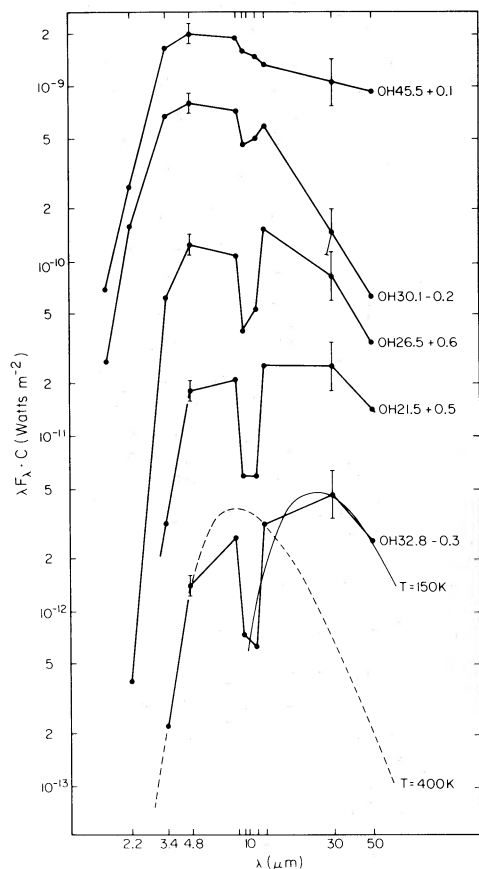


FIG. 1.—Infrared energy distributions for five very red OH/IR stars, 1978 July. The multiplicative constant on the y-axis has the following value for each source: OH 45.5+0.1 ($C = 265$); OH 30.1-0.2 (42); OH 26.5+0.6 (1); OH 21.5+0.5 (2.2); OH 32.8-0.3 (0.55).

that the OH maser emission is pumped radiatively by infrared photons (see also Harvey *et al.* 1974). Two infrared pumping schemes have been put forward for 1612 MHz OH masers, one involving vibrational excitation at $2.8 \mu\text{m}$ (Litvak 1969; Litvak and Dickinson 1972) and the other involving rotational excitation, primarily at $35 \mu\text{m}$ (Elitzur, Goldreich, and Scoville 1976). EB have shown quantitatively that the vibrational pump is unlikely for these sources, essentially because they are so faint at $2.8 \mu\text{m}$. The present data, which include measurements at far-infrared wavelengths, provide a direct quantitative test of the rotational pump model.

This is done by comparing the number of OH photons emitted per second, $n(\text{OH})$, with the number of infrared photons available to be absorbed per second in the $35 \mu\text{m}$ rotational transitions, $n(\text{IR})$.² The

² The present data show somewhat more flux at the wavelength of the $53 \mu\text{m}$ OH rotational transition, which also contributes to the population inversion, than was included in the calculation of Elitzur, Goldreich, and Scoville (1976). The $35 \mu\text{m}$ pumping should still be dominant for these sources, however, and the excess $53 \mu\text{m}$ radiation does not affect the conclusion that the maser is pumped in the rotational transitions (Scoville, private communication).

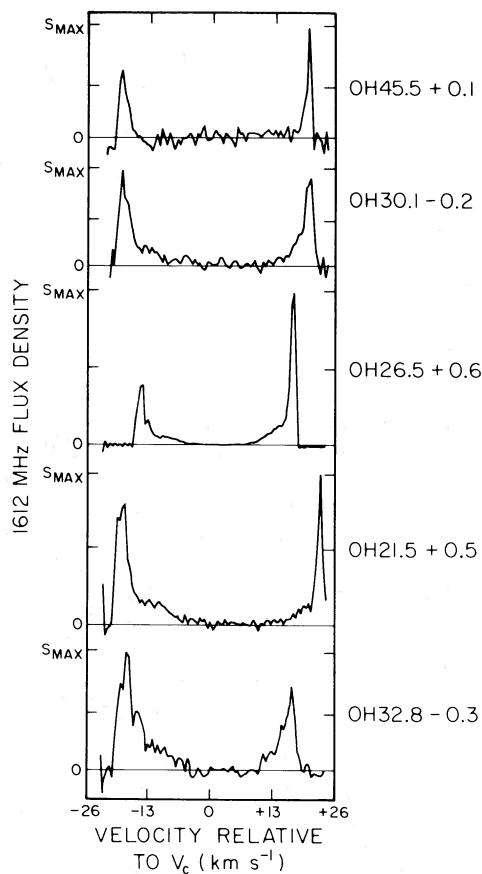


FIG. 2.—1612 MHz OH emission spectra for five very red OH/IR stars, 1978 July. The values of V_c (LSR) and S_{max} for the five stars are: OH 45.5+0.1 ($V_c = 17.3 \text{ km s}^{-1}$, $S_{\text{max}} = 12 \text{ Jy}$); OH 30.1-0.2 (34.1 km s^{-1} , 15 Jy); OH 26.5+0.6 (10.6 km s^{-1} , 400 Jy); OH 21.5+0.5 (99.4 km s^{-1} , 26 Jy); OH 32.8-0.3 (44.7 km s^{-1} , 17 Jy).

pump efficiency, $\epsilon = n(\text{OH})/n(\text{IR})$, must be less than 1 for the pumping model to be viable, because each OH photon requires at least one pump photon. A detailed discussion of the estimation of ϵ is given by EB. Their arguments show that, in the absence of a detailed model, it is plausible to relate ϵ to the observed peak OH and $35 \mu\text{m}$ flux densities, $S_\nu(\text{OH})$ and $S_\nu(35 \mu\text{m})$, by

$$\epsilon = \frac{S_\nu(\text{OH})}{S_\nu(35 \mu\text{m})}. \quad (1)$$

The efficiency ϵ has been computed from this relation for the data of 1978 July; the results are listed in column (1) of Table 3. The value of $S_\nu(35 \mu\text{m})$ was found by interpolation between the measured $30 \mu\text{m}$ and $50 \mu\text{m}$ flux densities. The computed efficiencies lie between 0.16 and 0.40, with a mean value of 0.27. Since $\epsilon < 1$ in each case, $35 \mu\text{m}$ pumping is feasible for these sources, as was previously suggested by Evans and Beckwith (1977) from an extrapolation of their near-infrared data.

The present data can be used with EB data of 1975

TABLE 3
EFFICIENCIES OF 35 μm PUMP

Source	1978 July ^a	1975 July ^b
OH 45.5+0.1.....	0.22	0.11-0.18
OH 30.1-0.2.....	0.40	0.38-0.39
OH 26.5+0.6.....	0.36	0.26-0.35
OH 21.5+0.5.....	0.19	0.22-0.31
OH 32.8-0.3.....	0.16	0.14-0.20

^a Based on present data.

^b Range extrapolated from Evans and Beckwith 1977 as described in text.

July, which include microwave and near-infrared but not far-infrared measurements, in order to investigate the variations of ϵ with the source brightness. In this analysis, unprimed quantities refer to the present observations, while primed quantities refer to those of 1975 July. It is assumed that the grain temperatures scale with the total luminosity \mathcal{L} of the source as $\mathcal{L}^{0.2}$, corresponding to a λ^{-1} dependence of the infrared emission efficiency, and that $\mathcal{L}'/\mathcal{L} = \mathcal{L}'(\lambda \leq 25 \mu\text{m})/\mathcal{L}(\lambda \leq 25 \mu\text{m})$; this is approximately correct since most of the luminosity of each source is at $\lambda \leq 25 \mu\text{m}$ (Table 1).

To set limits on the change in the 35 μm flux density, it is useful to consider the source of the 35 μm radiation. If the 35 μm radiation comes primarily from cold grains (those with temperature $\sim T_F$), then $S_\nu(35 \mu\text{m})$ depends exponentially on the grain temperature. If the 35 μm radiation comes primarily from hot grains with $T \approx T_N$, then $S_\nu(35 \mu\text{m})$ depends linearly on grain temperature. Thus, if $\mathcal{L}' > \mathcal{L}$,

$$\frac{B_\nu[35 \mu\text{m}, T_F(\mathcal{L}'/\mathcal{L})^{0.2}]}{B_\nu(35 \mu\text{m}, T_F)} > \frac{S_\nu'(35 \mu\text{m})}{S_\nu(35 \mu\text{m})} > (\mathcal{L}'/\mathcal{L})^{0.2} > 1. \quad (2a)$$

Here $B_\nu(\lambda, T)$ is a Planck function. If $\mathcal{L}' < \mathcal{L}$, the limits reverse:

$$\frac{B_\nu[35 \mu\text{m}, T_F(\mathcal{L}'/\mathcal{L})^{0.2}]}{B_\nu(35 \mu\text{m}, T_F)} < \frac{S_\nu'(35 \mu\text{m})}{S_\nu(35 \mu\text{m})} < (\mathcal{L}'/\mathcal{L})^{0.2} < 1. \quad (2b)$$

The limits calculated from equations (2a) and (2b) have been used with the 1975 July OH observations to compute a range of values for the pumping efficiency ϵ' . The results are tabulated in Table 3, and Figure 3 is a plot of $S_\nu(\text{OH})$ versus $S_\nu(35 \mu\text{m})$ for all sources, including the 1978 and the 1975 data. Note that the extrapolated values of ϵ' lie in the range 0.11-0.39, and that in no case does an extrapolated value of ϵ' differ by more than a factor of 2 from the directly measured ϵ . Therefore, the inferred efficiency for pumping by 35 μm photons appears to be fairly constant as the sources vary.

The results shown in Table 3 and Figure 3 are in good agreement with the pumping model put forward

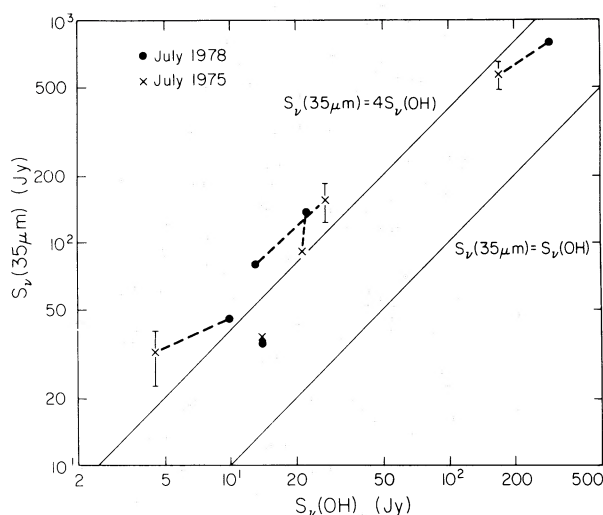


FIG. 3.—A comparison of the 35 μm and 1612 MHz OH flux densities for the five sources. The error bar for the 1975 July data gives the uncertainties in the extrapolated 35 μm flux for that epoch (see text). For 35 μm pumping to operate requires $S_\nu(35 \mu\text{m}) > S_\nu(\text{OH})$; $S_\nu(35 \mu\text{m}) \approx 4S_\nu(\text{OH})$ is predicted by the detailed model of Elitzur, Goldreich, and Scoville (1976).

by Elitzur, Goldreich, and Scoville (1976). In this model the maser is saturated, so that ϵ is independent of the source luminosity; the present results are consistent with this. Additionally, in the model of Elitzur *et al.* the pumping efficiency $\epsilon \approx 0.25$, comparable with the measured and extrapolated values in Table 3. Thus the results of this experiment strongly support the hypothesis that the 1612 MHz maser emission is pumped by 35 μm photons.

c) Formation of the 10 μm Silicate Feature

The present results suggest that the 10 μm silicate absorption features seen in the spectra of OH 21.5+0.5, OH 26.5+0.6, OH 30.1-0.2, and OH 32.8-0.3 are produced by the effects of temperature gradients in a thick circumstellar shell (Kwan and Scoville 1976). In this model the radiation seen in the core of the silicate feature at 10 μm is due to emission from cooler material further out in the shell than that which produces the adjacent continuum. The strongest evidence for this hypothesis is implicit in Figure 1, where the energy distributions are arranged in order of increasing depth of the silicate feature. For the four sources with silicate features, the apparent depth of the silicate feature is inversely correlated with the overall temperature of the source, as characterized, for example, by the ratio of 3.4 μm to 30 μm flux density. A correlation of this type is predicted by Kwan and Scoville (1976) for sources in which the silicate feature arises in the circumstellar shell. Its occurrence in this sample of sources supports the work of Forrest *et al.* (1978) who arrived at a similar conclusion based on their observation that, for OH 26.5+0.6, the apparent depth of the silicate feature is inversely correlated with the luminosity of the source.

A correlation between the depth of the silicate feature and the color temperature of the source qualitatively similar to that described above might also arise if the OH/IR stars are viewed through thick dust clouds which produce appreciable extinction both in the silicate feature and in the continuum at shorter wavelengths. The absence of a peak in the luminosity of these sources at far-infrared wavelengths shows, however, that they are not embedded in extended absorbing dust clouds such as those found in regions of star formation, which could produce a silicate feature by altering the spectrum of an embedded compact object (Pipher and Soifer 1976). EB have already shown, additionally, that the absence of strong 2.6 mm CO emission from the positions of these sources makes it unlikely that the silicate features are produced in intervening clouds along the line of sight. Finally, the result of Forrest *et al.* (1978) quoted above is also inconsistent with this hypothesis.

V. DISCUSSION OF DISTANCE-DEPENDENT QUANTITIES

a) Distance Estimates

The distances to these OH/IR stars can be determined only by indirect arguments. EB suggested the use of kinematic distances based on galactic rotation and found in particular that the near kinematic distances gave reasonable values for the infrared luminosities. The validity of this procedure is established by the work of Baud (1978), who has presented a statistical analysis of observations of over one hundred 1612 MHz masers which show the characteristic double-peaked profile. He finds that sources which have $\Delta V \gtrsim 29 \text{ km s}^{-1}$, as do those studied here, are closely confined to the galactic plane and follow the galactic rotation law, so that kinematic distances can be used.

Baud also presents a luminosity distribution which shows that the number of sources with a given OH luminosity, $N(\mathcal{L}_{\text{OH}})$, decreases approximately as $\mathcal{L}_{\text{OH}}^{-1.5}$, so that weak sources are much more common than strong ones. Four of the present five sources would be at least an order of magnitude more luminous in the OH line at their far kinematic distance than at their near kinematic distance. Furthermore, the OH luminosities derived using the far kinematic distances are unusually high compared with those of other known OH sources. The near kinematic distance (Table 4) is therefore adopted for each object.

b) Luminosities and Mass Loss Rates

The distance estimates permit the determination of the infrared luminosity \mathcal{L} of the sources, which ranged between $2.4 \times 10^3 \mathcal{L}_{\odot}$ and $4.8 \times 10^4 \mathcal{L}_{\odot}$ for 1978 July (see Table 4). For the purposes of evaluating mass loss rates, it is useful to have an estimate of the mean luminosity \mathcal{L}_M . This has been obtained from the time

TABLE 4
LUMINOSITIES AND MASS LOSS RATES

Source	D (kpc) ^a	\mathcal{L} (\mathcal{L}_{\odot}) ^b	\mathcal{L}_M (\mathcal{L}_{\odot}) ^c	\dot{M} ($\mathcal{M}_{\odot} \text{ yr}^{-1}$)
OH 45.5+0.1.....	2.1	2.5×10^3	2.2×10^3	5×10^{-6}
OH 30.1-0.2.....	3.1	1.1×10^4	1.1×10^4	3×10^{-5}
OH 26.5+0.6.....	1.8	3.2×10^4	2.5×10^4	7×10^{-5}
OH 21.5+0.5.....	7.5	4.8×10^4	3×10^4	7×10^{-5}
OH 32.8-0.3.....	3.9	6.5×10^3	1.8×10^4	5×10^{-5}

^a Near kinematic distance (see text).

^b Luminosity in 1978 July.

^c Mean luminosity based on all infrared data.

history of the infrared flux at the wavelength (typically either 4.8 μm or 12.5 μm) where the luminosity of each source peaks.

If the circumstellar material is accelerated to its final velocity by radiation pressure on dust grains, the mean mass loss rate \dot{M} is (Salpeter 1974; Forrest *et al.* 1978)

$$\dot{M} = \left(\frac{\tau_r}{cV} \right) \mathcal{L}_M, \quad (3)$$

where V is the observed final velocity, which is taken to be $\Delta V/2$, c is the velocity of light, and τ_r is the effective radiation pressure optical depth through the shell. For the optically thick shells under consideration here, $\tau_r > 1$, but it is unlikely to be much greater than 1 unless the grains have a high albedo. Thus a value $\tau_r = 2$ is chosen for the numerical estimates. The mass loss rates (Table 4) are found to be well in excess of $10^{-5} \mathcal{M}_{\odot} \text{ year}^{-1}$ for four of the five stars and close to $10^{-4} \mathcal{M}_{\odot} \text{ year}^{-1}$ in several cases. These mass loss rates are one to two orders of magnitude greater than those derived by Gehrz and Woolf (1971) from infrared observations of M stars with thinner dust shells than those studied here.

c) Nature of the Underlying Stars

Baud's (1978) work at radio wavelengths shows that the maser sources with $\Delta V \gtrsim 29 \text{ km s}^{-1}$ (which includes the present sample) have the kinematic characteristics of Population I objects. On the basis of kinematic arguments alone, he suggests that these objects could be identified either as luminous Mira variables or as M supergiants. Most visible OH/IR stars fall into these classes (Hyland *et al.* 1972; Hyland 1974). It is important to note, therefore, that the mean luminosities of the sources measured here, which range up to $3 \times 10^4 \mathcal{L}_{\odot}$, are consistent with these identifications. The average luminosity of Mira variables extends up to $\sim 2 \times 10^4 \mathcal{L}_{\odot}$ (Cahn and Wyatt 1978), while the luminosities of M supergiants range upward from $2.5 \times 10^4 \mathcal{L}_{\odot}$ (Lee 1970; Hyland, Thomas, and Robinson 1978). If these objects are Mira variables, their high luminosities and mass loss rates imply that they may be among the most extreme members of this

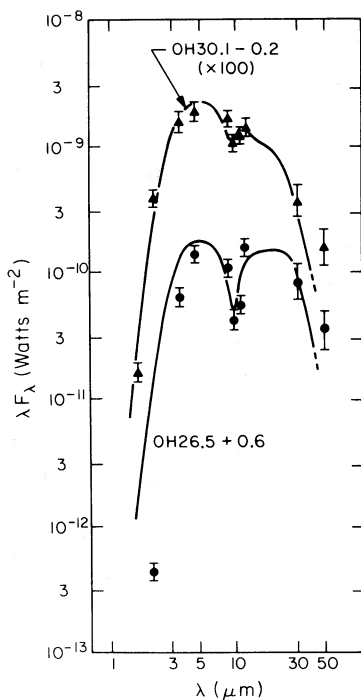


FIG. 4.—The observed infrared energy distributions of OH 26.5 + 0.6 and OH 30.1 – 0.2 (data points) are compared with two of the model calculations (solid curves) presented by Jones and Merrill (1976).

class. It may be possible to make definite identifications for some of the sources by searching for photospheric H₂O absorption at 1.9 μm , which is much stronger in Mira variables than in M supergiants (Hyland 1974).

VI. PROPERTIES OF THE CIRCUMSTELLAR SHELLS

a) Shell Parameters

Lower limits to the masses and radii of the circumstellar dust shells can be derived by comparing the data with a series of models presented by Jones and Merrill (1976), who have calculated the energy distributions of the infrared radiation from spherical circumstellar silicate dust shells with a range of opacities. Their models consist of a central star with $T = 2400$ K and shells which extend to 20 or 100 stellar radii, at which distance the grain temperatures have fallen to between 200 and 100 K. Figure 4 compares two of their model calculations with the observed energy distributions of OH 26.5 + 0.6 and OH 30.1 – 0.2. In these two cases, as for the other sources observed, the observations in the 10 μm range where most of the luminosity of the star emerges can be fit moderately well by one of their models. Because the models are truncated at $\lesssim 100$ stellar radii, they do not include material at very large distances from the star. Note that any such material would be too cold to radiate at 10 μm ; additionally, if the dust density decreases radially outward, the cold

material will not contribute significantly to the opacity in the 10 μm silicate feature. Thus cold material could be added beyond the outer boundary of the model shells without destroying the quality of the fit in the 10 μm region shown in Figure 4. The presence of such material is strongly suggested by the present observations which show, for each source, considerably more far-infrared radiation than predicted by the model which best fits the near-infrared data.

The quality of the fit shown in Figure 4 suggests that the best-fit model for each source is indicative of the radius and dust mass of the inner portion of the shell which produces the 10 μm radiation. This radius and mass are lower limits to the total mass and extent of the entire shell because of the truncation described above. The parameters which define the best fit model together with the radius of the model shell, R_M , and the mass of dust, \mathfrak{M}_D , within R_M , are given for each source in Table 5. In computing \mathfrak{M}_D from the model parameters, a value $3 \times 10^3 \text{ cm}^2 \text{ gm}^{-1}$ is taken for K , the mass opacity in the core of the 10 μm silicate feature (Hunt, Wisherd, and Bonham 1950; Friedmann, Gürtler, and Dorschner 1979). The minimum radii R_M range from 10^{15} to 5×10^{16} cm, while the minimum dust masses \mathfrak{M}_D lie between 10^{-6} and a few times $10^{-4} \mathfrak{M}_\odot$.

The excess long wavelength radiation shown in Figure 4 suggests outer shell radii and total masses larger than the lower limits given in Table 5, but the present observations do not permit a good determination of the true extent of the shell. This problem is illustrated by the results for OH 26.5 + 0.6. The minimum model radius $R_M = 3 \times 10^{16}$ cm, but the 30" diameter beam includes material out to a distance $R_0 = 4 \times 10^{17}$ cm from the star. If the mass loss has been steady for a time $R_0/V = 9 \times 10^3$ years, the mass (dust plus gas) within R_0 would be $\sim 0.6 \mathfrak{M}_\odot$. A simple extrapolation of the model out to radius R_0 leads to a predicted 45–130 μm flux of $3 \times 10^{-11} \text{ W m}^{-2}$. In view of the uncertainties in the measurement and the extrapolation, this estimate agrees with the observed 45–130 μm flux of $1.5 \times 10^{-11} \text{ W m}^{-2}$. The density and temperature structure of the model shell are such, however, that most of the energy received through the broad 45–130 μm passband is at the short wavelength end of the band and comes from material well within the extreme radius R_0 . Similar results are obtained for the other sources with the possible exception of OH 45.5 + 0.1. In that case, however, the 50 μm measurements may be contaminated by a contribution from the adjacent H II region G 45.5 + 0.1 (Zeilek, Kleinmann, and Wright 1975). For the other sources, the data are consistent with shells extending smoothly out to the limiting radius included within the 30" measuring aperture; these shells could be one to two orders of magnitude more massive than the lower limits given in Table 5. The data do not, however, require shells more than a few times larger and more massive than the lower limits given in Table 5. Observations of the flux longward of 100 μm are

TABLE 5
MODEL PARAMETERS AND DUST-TO-GAS RATIOS

SOURCE	MODEL PARAMETERS ^a						$f = \mathfrak{M}_D/\mathfrak{M}_M \equiv$ Dust-to-Gas Ratio by Mass
	n	τ	x	R_M (cm)	\mathfrak{M}_D (\mathfrak{M}_\odot)	\mathfrak{M}_M^b (\mathfrak{M}_\odot)	
OH 45.5+0.1	2	6	0.05	1.7×10^{15}	1.7×10^{-6}	1.7×10^{-4}	0.010
OH 30.1-0.2	2	6	0.05	3.5×10^{15}	7.6×10^{-6}	2.0×10^{-3}	0.004
OH 26.5+0.6	1.5	6	0.01	3.0×10^{16}	4.1×10^{-4}	5.0×10^{-2}	0.008
OH 21.5+0.5	1.5	6	0.01	3.6×10^{16}	6.1×10^{-4}	4.5×10^{-2}	0.014
OH 32.8-0.3	1	6	0.01	1.3×10^{16}	2.5×10^{-4}	1.4×10^{-2}	0.018

^a Parameters of circumstellar shell model presented by Jones and Merrill 1976 which gives best fit (by eye) to energy distribution observed in 1978 July. Parameters are: n = exponent of dust density distribution ($\rho(r) \propto r^{-n}$); τ = optical depth of shell in the core of the silicate feature at $10 \mu\text{m}$; x = inner shell radius/outer shell radius; R_M = outer shell radius of model calculated using distance and luminosity given in Table 4; \mathfrak{M}_D = mass of dust in shell.

^b $\mathfrak{M}_M = \mathfrak{M}R_M/V$ = total mass accumulated within R_M if mass loss has been steady for time R_M/V .

required to obtain better estimates of the shell radii, masses and lifetimes. Such estimates are necessary to an understanding of the significance of the current high mass loss phase for the evolution of these stars.

b) Dust-to-Gas Ratio

The dust-to-gas ratio in the inner portion of the shell can be estimated by comparing the mass of dust \mathfrak{M}_D within the radius R_M (Table 5) with the gas mass \mathfrak{M}_T expected to have accumulated within R_M under the assumption that the mass loss has proceeded at its present rate for a time $t_M = R_M/V$. Then $\mathfrak{M}_T \equiv \mathfrak{M}t_M = \mathfrak{M}R_M/V$, or, from equation (3),

$$\mathfrak{M}_T = \frac{R_M \mathfrak{Q}_M}{cV^2} \tau_r. \quad (4)$$

For each source the value of \mathfrak{M}_T and the inferred dust-to-gas ratio $f \equiv \mathfrak{M}_D/\mathfrak{M}_T$ are also included in Table 5. The value of f is moderately sensitive to the observed and adopted source parameters:

$$f \equiv \frac{\mathfrak{M}_D}{\mathfrak{M}_T} \propto \frac{V^2}{F_{\text{obs}}^{0.5} D \tau_r K}, \quad (5)$$

where F_{obs} is the total infrared flux observed at the Earth, D is the distance to the source, and the other parameters are defined above. For each source a value of f is found lying between 0.004 and 0.018; values for the dust-to-gas ratio in the general interstellar medium typically lie in this range. The general picture of these objects presented here is supported by the reasonable range of values found for f .

c) Radial Variation of Dust Density

Those objects with deep silicate features—OH 21.5+0.5, OH 26.5+0.6, and OH 32.8-0.3—seem to be better fitted by the models with dust density $\rho(r)$ varying radially as $r^{-1.5}$ or r^{-1} than by the r^{-2} models (Table 5). This result is demonstrated in Figure 4; the curve fit through the OH 30.1-0.2 data is a typical r^{-2} model. It would be a very poor fit to the OH 26.5+0.6 data, which are fit well by an $r^{-1.5}$ dust distribution.

This is of interest because an r^{-2} or steeper dependence of the total matter density is expected in the steady state if the circumstellar material is accelerated as it moves away from the star (Goldreich and Scoville 1976). It is clear physically why it is difficult to reproduce the breadth of the energy distribution (roughly comparable amounts of flux at $4.8 \mu\text{m}$ and $30 \mu\text{m}$) and the depth of the silicate feature observed in these sources with an optically thick model with $\rho(r) \propto r^{-2}$. If the dust density varies as r^{-2} , the opacity due to dust is high only at the center of the shell. Thus most of the power is radiated by grains concentrated toward the center of the shell which have roughly the same temperature, and a relatively narrow energy distribution results. A similar effect has been analyzed by Harvey, Thronson, and Gatley (1979) for optically thin circumstellar shells; it should be more marked when the shells are optically thick, as is true in the present case. The silicate feature appears to be weak in the r^{-2} case because the temperature contrast between the grains emitting in the core of the silicate feature and those emitting in the adjacent continuum is reduced. These arguments suggest tentatively that the apparent deviations of the data from an r^{-2} density gradient may not be an artifact of the particular models under consideration and that the dust density in the shells around objects such as OH 26.5+0.6 may decrease radially more slowly than r^{-2} , at least over the central $\sim 10^{16}$ cm. If this result is confirmed by further work, the slow decrease in dust density could be due to dynamic effects, such as variations with time of the mass loss rate, or it could be suggestive of continued grain growth as the material moves outward from the star. In the model put forward by Goldreich and Scoville (1976), for example, the gas-grain collision time is comparable to or shorter than the dynamical time scale for radii $\lesssim 10^{16}$ cm, so grain growth could, in principle, continue out to this radius.

VII. CONCLUSIONS

Simultaneous far-infrared, near-infrared, and 1612 MHz OH maser emission observations have led to the following conclusions concerning the properties

of five very red OH/IR stars from the list of Evans and Beckwith (1977):

(1) The results support the hypothesis that the maser emission is pumped in the rotational transitions, primarily at $35\ \mu\text{m}$. A strong correlation between $35\ \mu\text{m}$ flux density and 1612 MHz flux density is seen, both across the sample and for a given object as it varies. The average number of $35\ \mu\text{m}$ pump photons available per OH photon radiated is ~ 4 under the simplest interpretation of the data; this is in good quantitative agreement with the detailed model for rotational pumping of Elitzur, Goldreich, and Scoville (1976).

(2) The far-infrared radiation ($\lambda \geq 25\ \mu\text{m}$) contributes a significant (up to 40%) but not overwhelming portion of the total power output of these sources. On the basis of kinematic estimates of the distances to the objects, the directly measured luminosities are found to be in the range $2.5 \times 10^3 L_{\odot}$ – $4.8 \times 10^4 L_{\odot}$, and the inferred time-averaged luminosities lie in the range $2.2 \times 10^3 L_{\odot}$ – $3 \times 10^4 L_{\odot}$. This range overlaps that of both the extreme Mira variables and the M supergiants; both classes of objects may be represented in the sample. These identifications are in agreement with the results of Baud's (1978) survey of 1612 MHz OH maser emission sources in the galactic plane.

(3) The mass loss rates, as inferred from the luminosities, dust shell opacities, and outflow velocities approach $10^{-4} M_{\odot} \text{ year}^{-1}$ in several cases. For the objects with the high mass loss rates, the shell masses are greater than $10^{-2} M_{\odot}$.

(4) Four of the five sources have definite $10\ \mu\text{m}$ silicate absorption features; for these four sources, the apparent depth of the silicate feature is inversely correlated with the color temperature. This correlation, plus the absence of strong far-infrared emission from these objects, suggests that the $10\ \mu\text{m}$ silicate absorption feature is formed within the circumstellar shell and is not due to absorption of radiation from a hot background source by an intervening cold cloud. Thus the apparent depth of the silicate feature in objects of this type cannot be used as the basis for an extinction estimate for the purposes of distance and/or luminosity determinations.

We thank B. Gurney, S. Hatchett, J. Hicks and the staff and crew of the Kuiper Airborne Observatory for assistance with the observations. Helpful conversations and comments on the manuscript were contributed by N. J. Evans, A. R. Hyland, D. Lester, G. Neugebauer, N. Z. Scoville, B. T. Soifer, C. M. Telesco, and especially, B. Baud and P. Goldreich. We also thank J. Frazer and H. Lanning for assistance with the observations at Mount Wilson. The infrared observations were supported by NASA grants NGR 05-002-281 and NGL 05-002-207 and NSF grant AST 77-20516A1. Research at the Owens Valley Radio Observatory is supported by NSF grant AST 77-00247.

REFERENCES

- Baud, B. 1978, Ph.D. thesis, University of Leiden.
 Becklin, E. E., Matthews, K., Neugebauer, G., and Willner, S. P. 1978, *Ap. J.*, **219**, 121.
 Beckwith, S., Evans, N. J., Becklin, E. E., and Neugebauer, G. 1976, *Ap. J.*, **208**, 390.
 Bowers, P. F. 1978, *Astr. Ap. Suppl.*, **31**, 127.
 Cahn, J. H., and Wyatt, S. P. 1978, *Ap. J.*, **221**, 163.
 Caswell, J. L., and Haynes, R. 1975, *M.N.R.A.S.*, **173**, 649.
 Elitzur, M., Goldreich, P., and Scoville, N. 1976, *Ap. J.*, **205**, 384.
 Evans, N. J., and Beckwith, S. 1977, *Ap. J.*, **217**, 729.
 Forrest, W. J., et al. 1978, *Ap. J.*, **219**, 114.
 Friedmann, C., Gürtler, J., and Dorschner, J. 1979, *Ap. Space Sci.*, **60**, 297.
 Gehrz, R., and Woolf, N. J. 1971, *Ap. J.*, **165**, 285.
 Goldreich, P., and Scoville, N. 1976, *Ap. J.*, **205**, 144.
 Harvey, P. M., Bechis, K. B., Wilson, W. J., and Ball, J. A. 1974, *Ap. J. Suppl.*, **27**, 331.
 Harvey, P. M., Campbell, M. F., and Hoffmann, W. F. 1978, *Ap. J.*, **219**, 891.
 Harvey, P., Thronson, H. A., and Gatley, I. 1979, *Ap. J.*, **231**, 115.
 Hunt, J. M., Wisherd, M. P., and Bonham, L. C. 1950, *Anal. Chem.*, **22**, 1478.
 Hyland, A. R. 1974, in *IAU Symposium No. 60, Galactic Radio Astronomy*, ed. F. Kerr and S. C. Simonson (Dordrecht: D. Reidel), p. 439.
 Hyland, A. R., Becklin, E. E., Frogel, J. A., and Neugebauer, G. 1972, *Astr. Ap.*, **16**, 204.
 Hyland, A. R., Thomas, J. A., and Robinson, G. 1978, *A.J.*, **83**, 20.
 Johansson, L. E. B., Anderson, C., Goss, W. M., and Winnberg, A. 1977, *Astr. Ap. Suppl.*, **28**, 199.
 Jones, T. W., and Merrill, K. M. 1976, *Ap. J.*, **209**, 509.
 Kwan, J., and Scoville, N. Z. 1976, *Ap. J.*, **209**, 102.
 Lee, T. 1970, *Ap. J.*, **162**, 217.
 Litvak, M. M. 1969, *Ap. J.*, **156**, 471.
 Litvak, M. M., and Dickinson, D. F. 1972, *Ap. Letters*, **12**, 113.
 Pipher, J. L., and Soifer, B. T. 1976, *Astr. Ap.*, **46**, 153.
 Salpeter, E. E. 1974, *Ap. J.*, **193**, 585.
 Schultz, G. V., Kreysa, C., and Sherwood, W. A. 1976, *Astr. Ap.*, **50**, 171.
 Telesco, C. M., Kleinmann, S., Harper, D. A., Loewenstein, R., and Moseley, S. H. 1980, in preparation.
 Telesco, C. M., and Harper, D. A. 1977, *Ap. J.*, **211**, 475.
 Winnberg, A., Goss, W. M., Höglund, B., and Johansson, L. E. B. 1973, *Ap. Letters*, **13**, 125.
 Zeilik, M., Kleinmann, D. E., and Wright, E. L. 1975, *Ap. J.*, **199**, 401.

S. BECKWITH: Department of Astronomy, Space Sciences Building, Cornell University, Ithaca, NY 14853

G. BERRIMAN, K. SELLGREN, and D. L. WHITING: Downs Laboratory of Physics, 320-47, California Institute of Technology, Pasadena, CA 91125

I. GATLEY: UK Infrared Telescope Unit, 900 Leilani Street, Hilo, HI 96720

M. W. WERNER: M/S 245-6, NASA Ames Research Center, Moffett Field, CA 94035